Tectonophysics 688 (2016) 1–10

Contents lists available at ScienceDirect

Tectonophysics

journal homepage: www.elsevier.com/locate/tecto

Crustal structure and fracture zone in the Central Basin of the South China Sea from wide angle seismic experiments using OBS

Aiguo Ruan [a,b], Xiaodong Wei [a,*], Xiongwei Niu [a], Jie Zhang [b], Chongzhi Dong [a], Zhenli Wu [a], Xinyang Wang [a]

[a] The Second Institute of Oceanography, State Oceanic Administration, Hangzhou 310012, China
[b] Department of Earth Sciences, Zhejiang University, Hangzhou 310027, China

ARTICLE INFO

Article history:
Received 14 January 2015
Received in revised form 25 August 2016
Accepted 15 September 2016
Available online 16 September 2016

Keywords:
Central basin of the SCS
Crustal structure
Fracture zone
Wide-angle seismic experiment using OBS
2D ray-tracing simulation

ABSTRACT

We present two E-W trending wide-angle seismic profiles (OBS2013-ZN, OBS2014-ZN), which cross the boundary (Zhongnan fault zone) between the east sub-basin and the southwest sub-basin of the South China Sea (SCS). We processed the data and used 2D ray-tracing to determine the oceanic crust thickness, velocity structures and Moho depth variations related to the fault zone. The simulated velocity models show that the oceanic basin of the SCS has a typical oceanic crust covered by a 1–2 km thick sediment layer with a velocity of 2.0–3.5 km/s. The crust has a thickness of 5–8 km, of which the oceanic layer 2 is 1.8–3 km thick, with velocity increasing downward from 4.3 km/s to 6.4 km/s, and the oceanic layer 3 is 3–5 km thick, with velocity increasing downward from 6.4 km/s–7.0 km/s. The Moho depth in the oceanic basin is approximately 6–7 km below seabed. The Moho discontinuity has a prominent upheaval zone with a low velocity of 7.6 km/s, whose location corresponds to the low velocity zone in oceanic layer 2. Our results suggest the presence of a NW-SE-trending fracture zone (40–60 km wide) rather than a major "Zhongnan fault" oriented N-S by connecting the upheaval portions of the Moho in the two profiles. The NW-SE orientation Zhongnan transform fault zone in our study area is consistent with the direction of opening of the South China Sea in the last stage of its evolution. This large transform fault zone connected and offset the spreading centers of the east and southwest sub-basin.

© 2016 The Authors. Published by Elsevier B.V. This is an open access article under the CC BY-NC-ND license (http://creativecommons.org/licenses/by-nc-nd/4.0/).

1. Introduction

Morphologically, very prominent structures in the SCS basin are two seamount chains located from 12°N to 16°N, coincident with two abandoned spreading ridges and separated by an offset near 116°E (Fig. 1). The Zhenbei-Huangyan (Scarborough) seamount chain is distributed along a nearly EW oriented spreading axis in the east sub-basin, while the Changlong-Zhongnan seamount chain is distributed along a NE oriented spreading axis in the southwest sub-basin. The fossil spreading ridge sections, seamount chains, and magnetic anomalies show a large offset and a change in general direction near 116°E, and the mechanism that separated the east sub-basin from the southwest sub-basin is one of the most important questions of the evolutionary history of the SCS. Although some authors have assumed that the boundary near 116°E is composed of major faults or fracture zones, their locations and trending directions are still unclear due to a lack of direct evidence. Taylor and Hayes (1980, 1983), followed by Ru and Piggot (1986), proposed that the E-W oriented magnetic anomalies in the east sub-basin terminate at major N-S trending fault zones. On the basis of morphological and geophysical data and seismic reflection profiles, Yao (1995) also proposed a major N-S trending fault, named Zhongnan fault, which extends nearly along the longitude of 116°E from the Pearl River mouth-valley, crosses the western central basin, Zhongnan seamount chain and Reed Bank Trough and finally reaches northeastern-most Borneo. He further suggested that Reed Bank in the south margin has a conjugate relationship with Dongsha Rise in the north margin (Yao et al., 1994). Similarly, on the basis of magnetic anomalies, Li and Song (2012) proposed a major fault between the northwest sub-basin and the northern part of the east sub-basin and connected it with the separating boundary between the east sub-basin and southwest sub-basin to form a major N-S fault. Franke (2013) postulated that the east sub-basin is separated from the southwest sub-basin by a NNW trending fracture zone between Macclesfield Bank and Reed Bank. In the interpretations given by Briais et al. (1993) based on magnetic anomaly analysis and Braitenberg et al. (2006) based on gravity data derived crystalline basement the spreading axis in the southwest sub-basin continues through the central basin near 116°E with no other faults than the spreading center transform faults.

However, previous studies were mainly based on magnetic data without crustal structure evidence, especially for deep structures. In

* Corresponding author.
E-mail address: xdwei_922@126.com (X. Wei).

http://dx.doi.org/10.1016/j.tecto.2016.09.022
0040-1951/© 2016 The Authors. Published by Elsevier B.V. This is an open access article under the CC BY-NC-ND license (http://creativecommons.org/licenses/by-nc-nd/4.0/).

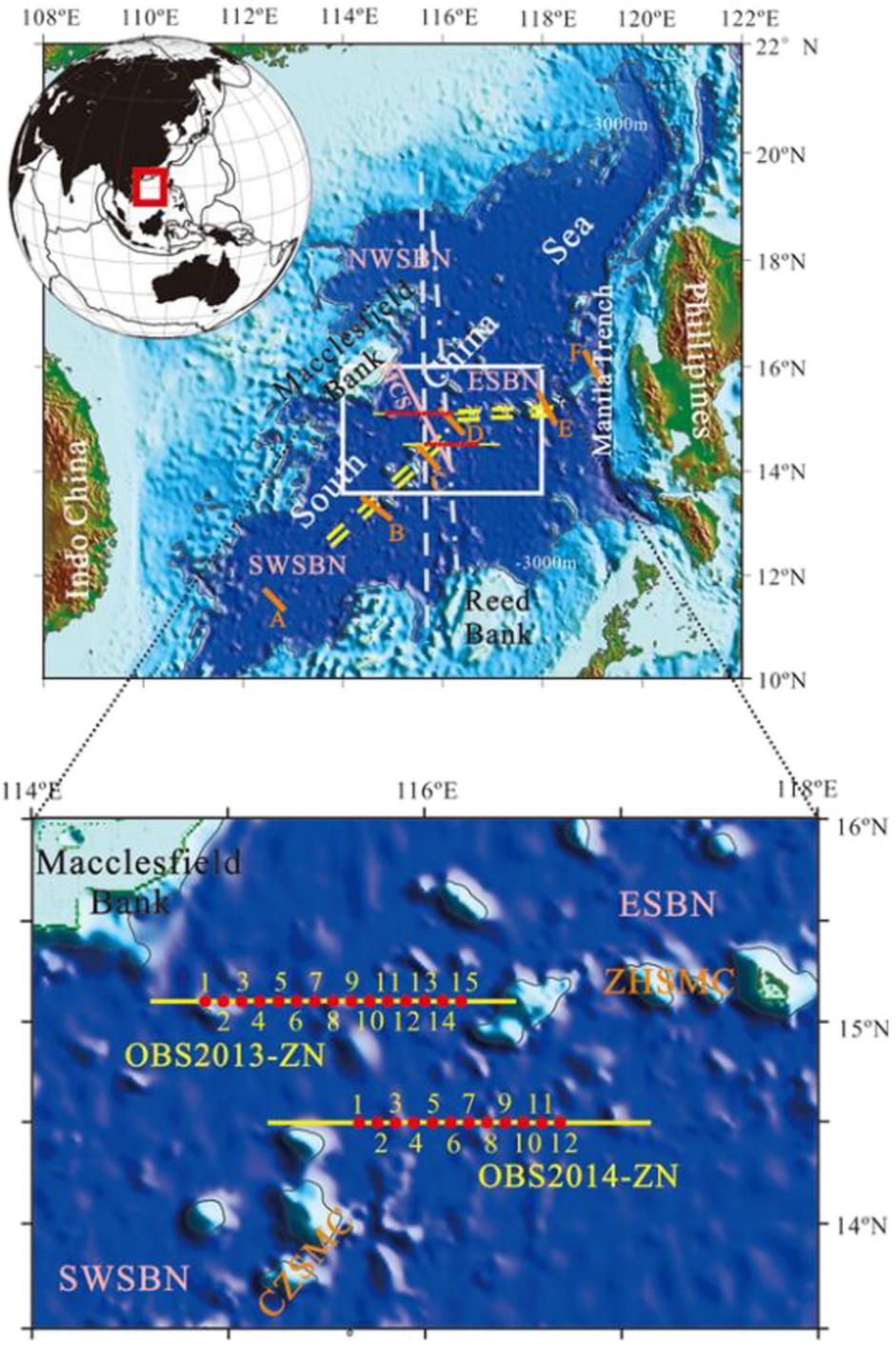

Fig. 1. Topography and bathymetry of the South China Sea region with the location of the sub-basins, seamounts, spreading centers and the postulated Zhongnan fault (The dashed line proposed by Yao (1995); the dash-dotted line proposed by Li et al., 2008). The pink solid line is a seismic reflection profile completed in the previous investigation shown in Fig. 12. The double yellow lines represent the fossil spreading ridge according to high-resolution bathymetry from Li et al. (2011). SWSBN = Southwest sub-basin, ESBN = East sub-basin, NWSBN = Northwest sub-basin, ZHSMC = Zhenbei-Huangyan (Scarborough) seamount chain, CZSMS = Changlong-Zhongnan seamount chain.

this paper we present two wide-angle seismic profiles (OBS2013-ZN and OBS2014-ZN), which cross the boundary (Zhongnan fault zone) between the east sub-basin and the southwest sub-basin (Fig. 1). We determined the oceanic crust thickness, P-wave velocity structures and Moho discontinuity using 2D ray-tracing to reveal shallow and deep signals related to major faults, to better understand the change in general direction of magnetic anomalies and spreading axes near 116°E as well as the dynamic process of the SCS seafloor spreading.

2. Geological setting

The SCS is a western Pacific marginal sea situated at the junction of the Eurasian, Pacific, and Indo-Australian plates, and geographically consists of the northern continental margin, the oceanic basin and the southern continental margin (Fig. 1). The sea basin has an oceanic crust (Ludwig et al., 1979) with water depth of 3500–4400 m and has been subdivided into the central/east sub-basin, northwest sub-basin

and southwest sub-basin (Hutchison, 1989; Li et al., 2008). Following the researches of Taylor and Hayes (1980, 1983) and Ru and Piggot (1986), further magnetic anomaly measurements and studies have indicated that the SCS oceanic basin was formed by poly-phase seafloor spreading but with various point of views in magnetic anomaly age and seafloor spreading rate (Briais et al., 1993; Yao et al., 1994; Sun. et al., 2009; Franke, 2013). Li et al. (2011) suggested that the first spreading stage was from 33.5 Ma to 25 Ma (magnetic anomaly C13-C8) in the east and northwest sub-basins, with a spreading direction of NNW-SSE. After a ridge jump of ~50 km to the south at 25 Ma (Briais et al., 1993), the second spreading stage started from 25 Ma to 16.5 Ma (magnetic anomaly C8-$C5_c$) in the east sub-basin and simultaneously started in the southwest sub-basin with a direction of NW-SE. The terminal age of spreading is ~15 Ma in the East Subbasin and ~16 Ma in the Southwest Subbasin (IODP Expedition 349 Scientists, 2014; Li et al., 2014) In the deep-sea basin there are numerous seamounts with ages of 13.8–3.5 Ma, indicating that another episode of magmatic activity occurred in the SCS after the cessation of seafloor spreading (Wang et al., 1984;Kudrass et al., 1986; Hékinian et al., 1989; Yan et al., 2008, 2014; Xu et al., 2012; Li et al., 2014).

In the study area the abandoned spreading ridges from southwest to northeast may be divided into three sections (Fig. 1). Section AB (300 km long) is of the ridge valley (40 km wide) surrounded by small seamounts linearly distributed on both banks. Along section BC (140 km long) ridge valley is relatively narrow and larger seamounts form a chain which is named Changlong-Zhongnan seamount chain. Section CD (90 km long) is an area absent of seamount where Zhongnan Fault is supposed to traverse. A NNW trending negative topography (−70 km wide) can be distinguished in this section. Section DE (180 km long) consists of the E-W trending Zhenbei-Huangyan (Scarborough) seamount chain and is absent of distinct ridge valley, which is the main portion of the east sub-basin spreading ridge. The volcaniclastic breccia and sandstone at IODP349 site U1431 (2014) are dated as late middle Miocene to early late Miocene (8–13 Ma), suggesting a 5 Ma duration of seamount volcanism starting a few million years after the cessation of seafloor spreading. Along section EF (−140 km long) seamount chain extends in NE direction to the Manila Trench. The OBS development area with water depth 3880- 4350 m has a crust of 4.4–8.8 km thick with Moho depth 6–7 km bellow seabed estimated by previous studies (Yao et al., 1994). The research area has a free-air gravity anomaly of 10 mGal (Li et al., 2011).

3. Seismic data

3.1. Data acquisition

The wide-angle seismic profile (OBS2013-ZN) located in the central basin of the SCS trending E-W along the latitude of 15.1°N was completed in April 2013 using fifteen OBS (three components and one hydrophone) at intervals of 10 km. The total shooting length was 203 km extended 30 km beyond the two end stations. The wide-angle seismic profile (OBS2014-ZN) was also located in the central basin of the SCS and trended E-W along the latitude of 14.5°N. It was completed in July 2014 using twelve OBS at intervals of 10 km. Its total shooting length was 210 km extended 50 km beyond the two end stations (Fig. 1). The same seismic source provided by R/V "*Shiyan 2*" was used for both experiments. An air gun array of 4 × 24.5 l was shot at a pressure of 120–130 kg/cm^2 every 120 s, and the average shooting interval was approximately 280 m. GPS was used to determine location and time during the OBS deployment and recovery, vessel navigation and air gun shooting. The four-component OBS data were sampled at intervals of 4 ms. Reflection seismic measurements were simultaneously recorded in a single channel seismic stream to obtain the seabed relief and sediment basement (Fig. 2, Fig. 3).

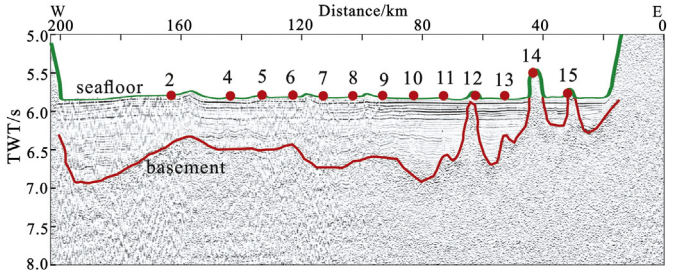

Fig. 2. The single channel seismic reflection section along the profile OBS2013-ZN. The solid circles represent OBS stations.

3.2. Single Channel seismic profiles

The single channel seismic data processing included band-pass filtering, surface consistent amplitude compensation, abnormal high amplitude noise suppression and geometric spreading correction. The processed seismic reflection profiles (Fig. 2, Fig. 3) show that the seafloor is flat with a water depth of 3880–4350 m. A number of small basement highs are distributed along the profiles. Correspondingly, the crystalline basement depth drastically varies the sediment is flat in the shallow portion but varies drastically in the deep portion, with a mean thickness <2 km (TWT < 1 s).

3.3. OBS data processing and phase picking

The OBS data processing included shot time correction, localization of shootings coordinates, OBSs coordinates correction, recorder time drift correction and data filtering (Ao et al., 2010). In addition, we also considered the influence of direction changes of the vessel relative to the antenna position of the GPS receiver. The final profile line was determined by a least squares calculation of the shot positions along the profile. The position of each station on the seafloor was roughly determined from a water depth measurement and was then modified by fitting the theoretical travel time of a direct water wave to the observed travel time. The frequency of the band-pass filter was 4–30 Hz, the reduced velocity was 8 km/s, and only the vertical component was used for P-wave velocity modeling in this paper. Seismic phases were identified and picked by initial travel time modeling and then re-determined during the inversion stage. Herein, the direct water wave is labeled Pw, the refracted wave from the sediment layer is labeled PsP, the refracted wave from the oceanic crust is labeled Pg, the reflected wave from the Moho discontinuity is labeled PmP, and the refracted wave from the upper mantle is labeled Pn.

3.3.1. Seismic sections and phase selection along profile OBS2013-ZN

The seismic data recorded by the OBSs along this line are generally of high quality, except for station No. 11. There were very few refraction and reflection phases from the sediment layer, and they were difficult to recognize due to the limited thickness of the sediment layer. Refraction phases Pg and Pn were observed at all stations, and reflection phases PmP were clearly observed at some stations but were difficult to identify at other stations. For example, in the seismic section of OBS06 (Fig. 4), PmP begins to appear near the offset of 15 km in the eastern branch but has no clear signals in the western branch. Subsequently, the Moho depth under this station is estimated to be ~10 km, and the eastern part is relatively shallow. Close to OBS06, the seismic section of OBS07 (Fig. 5) has weak amplitude but clear phases PmP in both branches. The refraction phases Pg were observed at all stations within relatively short distances, which indicate that the oceanic crust is thin. The phase Pg travel times varied horizontally with the distribution of seamounts. In addition to the strong constraints from the phases

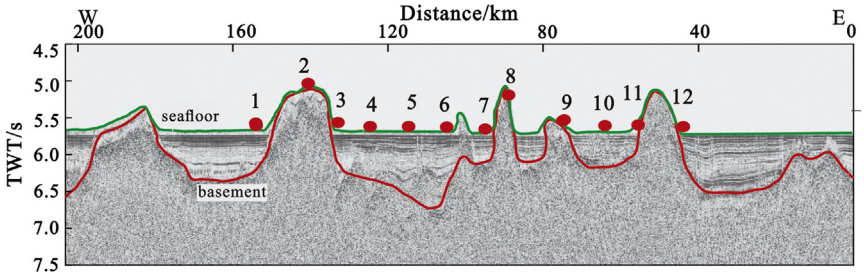

Fig. 3. The single channel seismic reflection section along the profile OBS2014-ZN. The solid circles represent OBS stations.

PmP, the phases Pn were also important for determining the Moho depth and the topmost velocity of the upper mantle. Because the oceanic basin has a thin crust, the phases Pn were the first arrivals at short distances easy to identify and could be traced for long distances. For example, in the seismic section of OBS10 (Fig. 6), the maximum offset of Pn appearance can be traced further than 100 km. The pick uncertainties and fitting errors of the seismic phases travel times along profile OBS2013-ZN are listed in Table 1.

3.3.2. Seismic sections and phase selection along profile OBS2014-ZN

The seismic data recorded by the OBSs along this line are generally of high quality, except for station No. 8. The refraction phases Pg and Pn were observed at all stations and the phases PmP were observed at most stations. For example, the seismic section of station OBS01 (Fig. 7) shows that the phases Pg were clearly influenced by seamounts and can be traced only over short distances because of the limited thickness of the oceanic crust. In this seismic section the phases PmP had high amplitude, but the phases Pn were relatively weak, which indicates that the Moho is relatively deep under this station. While the phases Pn in the seismic section of station OBS05 (Fig. 8) can be traced at the offset of 70 km only in the eastern branch but can be traced in both branches in the seismic section of station OBS09 (Fig. 9) The pick uncertainties and the travel time fitting errors of the seismic phases along profile OBS2014-ZN are also listed in Table 1.

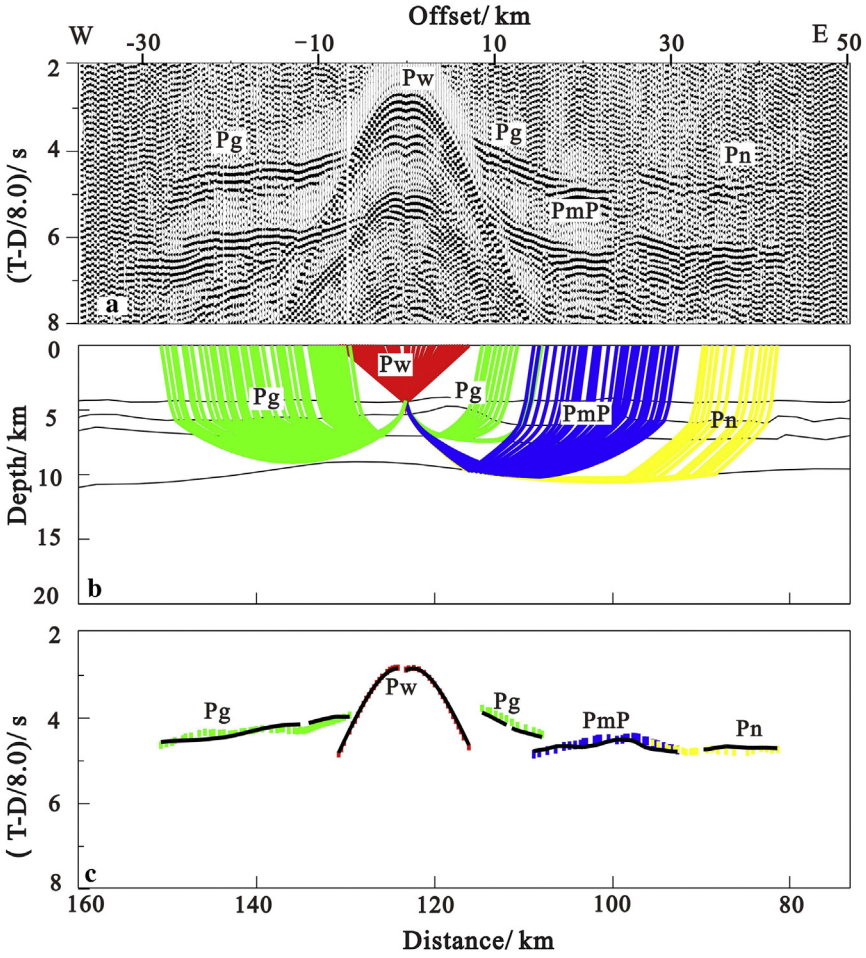

Fig. 4. The seismic section of station OBS06 in the line OBS2013-ZN (reduced velocity is 8.0 km/s). (a) seismic section, (b) ray-tracing, (c) travel time fitting. The seismic phases in Fig. 4 (a) are illustrated as text, seismic rays differently colored in Fig. 4 (b) represent different traveling paths corresponding to the seismic phases in Fig. 4 (a). The black dotted lines represent downward seabed, crustal interface and Moho respectively. In the fitting results (Fig. 4 (c)), the black circus represent theoretical travel time, the vertical color bars represent picked travel time corresponding to the seismic phases in Fig. 4 (b), the length of color bar is two times of phase picking error (Zelt and Smith, 1992).

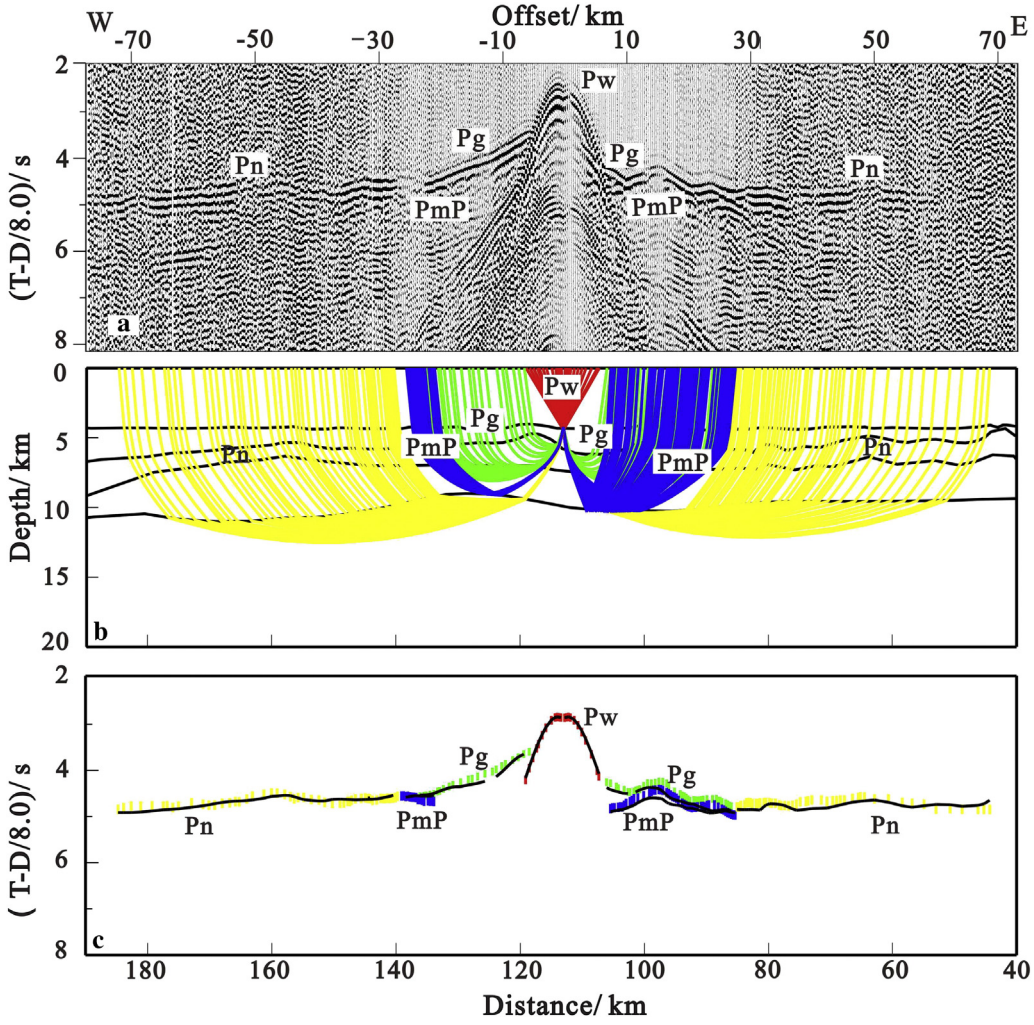

Fig. 5. The seismic section of station OBS7 in the line OBS2013-ZN (reduced velocity is 8.0 km/s). (a) seismic section, (b) ray-tracing, (c) travel time fitting, illustrated as Fig. 4.

4. Crustal structures

4.1. Modeling approach

Both initial models of the two profiles were the same and consisted of five layers, as follows: (1) 1.5 km/s sea water layer; (2) 0–2 km thick sediment layer with velocities of 1.8 km/s at the top and 3.8 km/s at the bottom (oceanic layer 1); (3) 2.0 km thick upper crust with velocities of 4.0 km/s at the top and 6.4 km/s at the bottom (oceanic layer 2); (4) 5 km thick lower crust with velocities of 6.4 km/s at the top and 7.0 km/s at the bottom (oceanic layer 3); (5) upper mantle with velocities of 8.0 km/s at the top and 8.2 km/s at a depth of 20 km. This model was based on the single channel seismic profiles simultaneously measured, global averages of oceanic crustal structure (White et al., 1992) and SCS seismic velocity models in previous studies (Ruan et al., 2011; Qiu et al., 2011). The two-dimensional velocity models were parameterized as sheared meshes beneath the seafloor. The horizontal node spacings were heterogeneously assigned based on the seabed relief and the distribution of basement highs revealed by the single channel seismic profiles, with a node spacing of 5–20 km for the sediment layer and the crust and 20 km for the upper mantle. Except for the water layer, the vertical node spacing was set to the layer thickness to maintain a constant vertical velocity gradient within each layer.

The velocity models were constructed using two-dimensional travel time modeling and inversion with the RayInvr code of Zelt and Smith (1992). The velocities and interfaces were initially adjusted manually by trial and error approach from the sediment to the mantle one station at a time. After the forward modeling, a damped least squares inversion was conducted with a node spacing of 0.5 km × 0.25 km, by taking the travel time error as the target function and keeping the layer interfaces fixed to obtain an optimized P-wave velocity model (Fig. 10a and Fig. 11a).

We used a statistical approach to estimate the seismic phase fitting errors (Table 1) and model uncertainties (Table 2). It shows that all of the phases have lower travel time root-mean-square (RMS) misfits with χ^2 values in the range of 1.0–1.9, which indicates that the simulated models were suitably parameterized and have high accuracy (Zelt and Smith, 1992). Furthermore, the ray densities of both profiles (Fig. 10c and Fig. 11c) show that the ray coverage on each interface was generally in the range of 20–70 times (at least 10 times), which indicates that the interfaces were strongly constrained and that the final models have high resolutions (Zelt, 1999).

4.2. P-wave velocity models

The simulated velocity models show that the SCS sea basin has a typical oceanic crust covered by a 1–2 km thick sediments layer with a

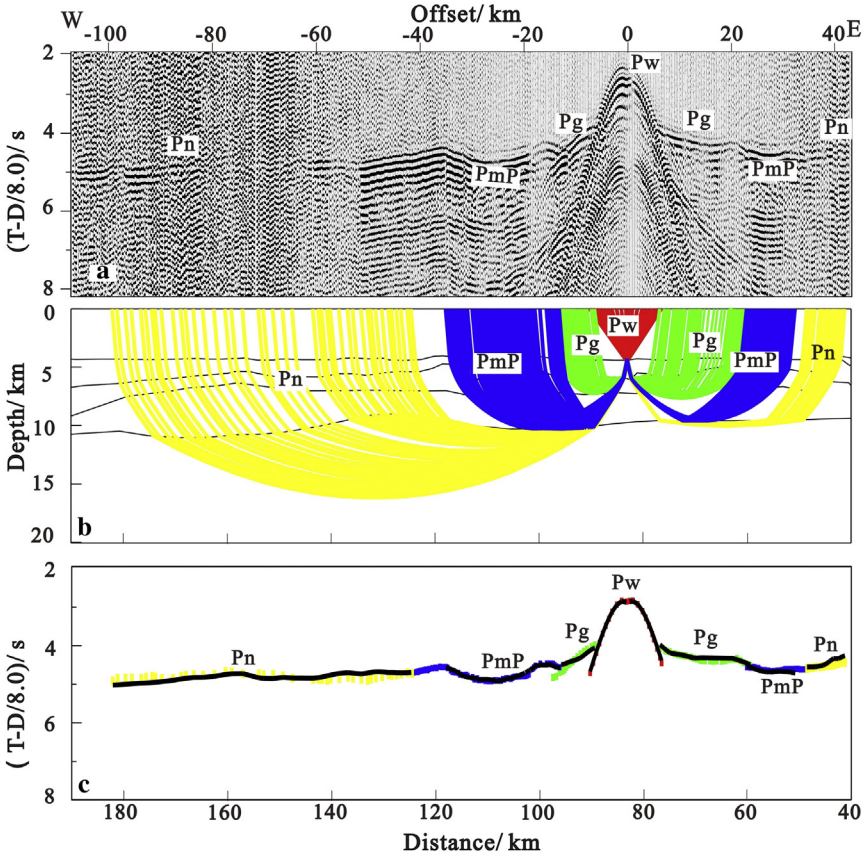

Fig. 6. The seismic section of station OBS10 in the line OBS2013-ZN (reduced velocity is 8.0 km/s). (a) seismic section, (b) ray-tracing, (c) travel time fitting, illustrated as Fig. 4.

velocity of 2.0–3.5 km/s. The crust has a thickness of 5–8 km, in which oceanic layer 3 (3–5 km thick) is thicker but has a smaller vertical velocity gradient than oceanic layer 2. The details of the two velocity models are now described.

(1) The velocity model of profile OBS2013-ZN is shown in Fig. 10a. Along the profile, some seamounts with low velocity emerge from the seabed, formed partly by unconsolidated volcaniclastics. The velocities of the sediment layer (1–2 km thick) increase downward from 1.8 km/s to 3.5 km/s with little horizontal variation. Oceanic layer 2 is 1.8 km–2.8 km thick, again with little horizontal variation, but it has a large vertical velocity gradient with velocity increasing downward from 4.3 km/s to 6.4 km/s. The velocity perturbation anomaly (Fig. 10b) indicates the presence of a low velocity zone in oceanic layer 2 under stations OBS03-OBS08. The interface between oceanic layer 2 and layer 3 is coincident with the 6.4 km/s isovelocity contour. Oceanic layer 3 has a prominent lateral variation in thickness, with a minimum thickness of 2.5 km under station OBS05, which gradually increases to the east and west. Oceanic layer 3 has a smaller vertical velocity gradient than that of oceanic layer 2, but at its bottom the velocity varies horizontally with minimum velocity of 6.8 km/s under station OBS06, which increases to 7.0 km/s to the east and west. The ray density distribution of the model (Fig. 10c) shows that the Moho discontinuity depth is well constrained by phases PmP, and the upper mantle velocity is also well constrained by phases Pn. The velocity model shows that the Moho is obviously upheaved under stations OBS04-OBS07, and, correspondingly, the velocity perturbation anomaly indicates the presence of a low velocity zone of 7.6 km/s at the upmost portion of the mantle under these stations.

(2) The velocity model of profile OBS2014-ZN is shown in Fig. 11a. The sediment layer has a prominent lateral variation in the thickness from zero to 2 km; Some seamounts that are distributed along the profile emerge from the seabed with low velocity, formed by unconsolidated volcaniclastics. Oceanic layer 2 has a prominent horizontal variation in thickness from 1.8 km to 3 km, with a horizontal variation velocity in its top part, and it shows a large vertical velocity gradient with velocity increasing downward from 4.3 km/s to 6.4 km/s. The velocity perturbation anomaly (Fig.11b) indicates the presence of a low velocity zone in oceanic layer 2 under stations OBS02-OBS09. Oceanic layer 3 has a clear lateral thickness variation, with a minimum thickness of 2.5 km in the center, which gradually increases eastward and westward to 5 km. At its bottom, the velocity varies horizontally with a minimum velocity of 6.8 km/s under station OBS07, which increases to 7.0 km/s to the east and west. It also shows that the Moho is obviously uplifting from 12 km deep on both sides to 10 km deep under stations OBS04-OBS08, and, correspondingly, the velocity perturbation anomaly indicates the

Table 1
Phases picks and fitting errors.

Profile	OBS2013-ZN			OBS2014-ZN		
Phases	No. of picks	RMS (ms)	χ^2	No. of picks	RMS (ms)	χ^2
Pw	1073	44	1.001	530	65	1.003
Pg	2241	97	1.457	901	105	1.621
PmP	783	99	1.450	378	110	1.860
Pn	1092	113	1.808	631	103	1.532
PsP	148	108	1.578			
Total	5337	100	1.311	2440	98	1.496

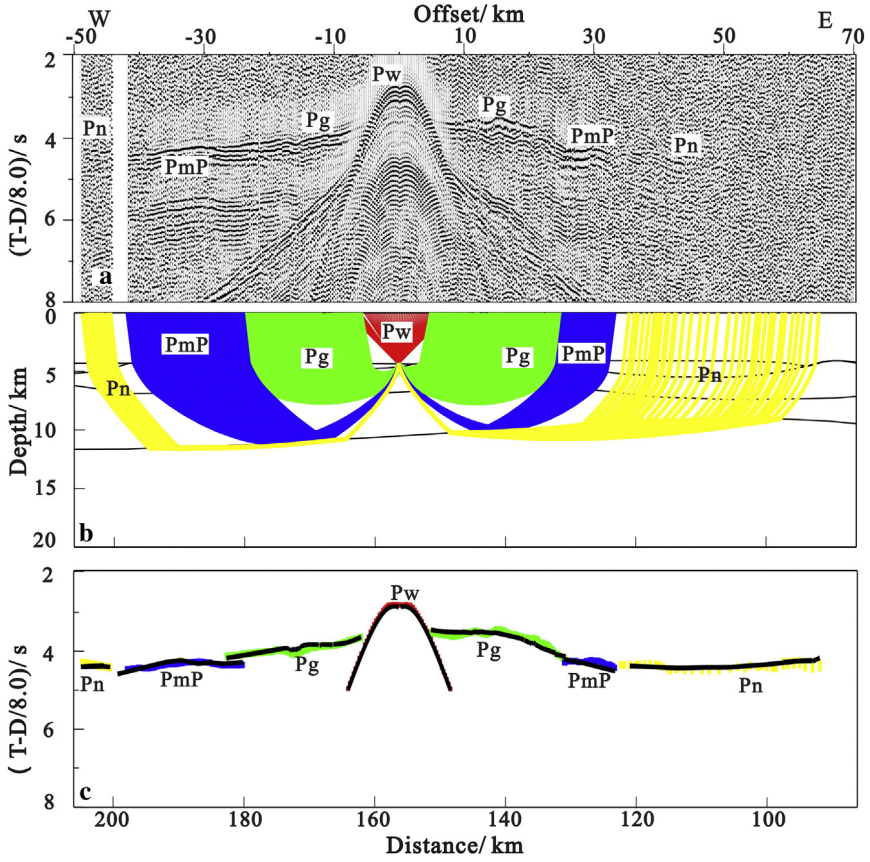

Fig. 7. The seismic section of station OBS01 in the line OBS2014-ZN (reduced velocity is 8.0 km/s). (a) seismic section, (b) ray-tracing, (c) travel time fitting, illustrated as Fig. 4.

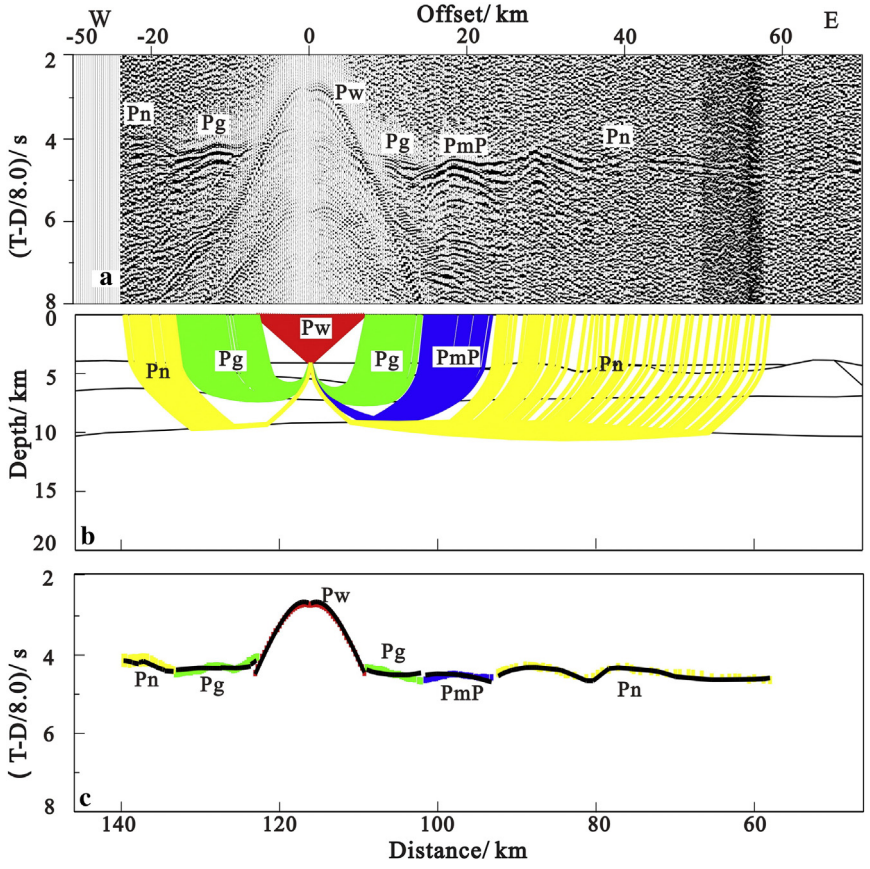

Fig. 8. The seismic section of station OBS05 in the line OBS2014-ZN (reduced velocity is 8.0 km/s). (a) seismic section, (b) ray-tracing, (c) travel time fitting, illustrated as Fig. 4.

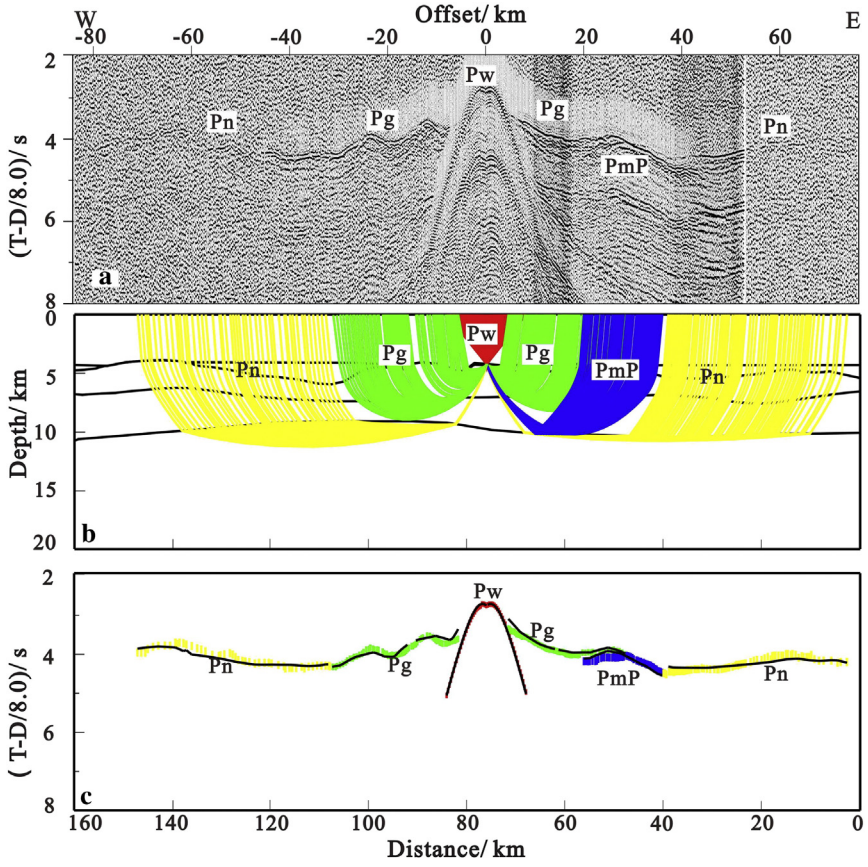

Fig. 9. The seismic section of station OBS09 in the line OBS2014-ZN (reduced velocity is 8.0 km/s). (a) Seismic section, (b) ray-tracing, (c) travel time fitting, illustrated as Fig. 4.

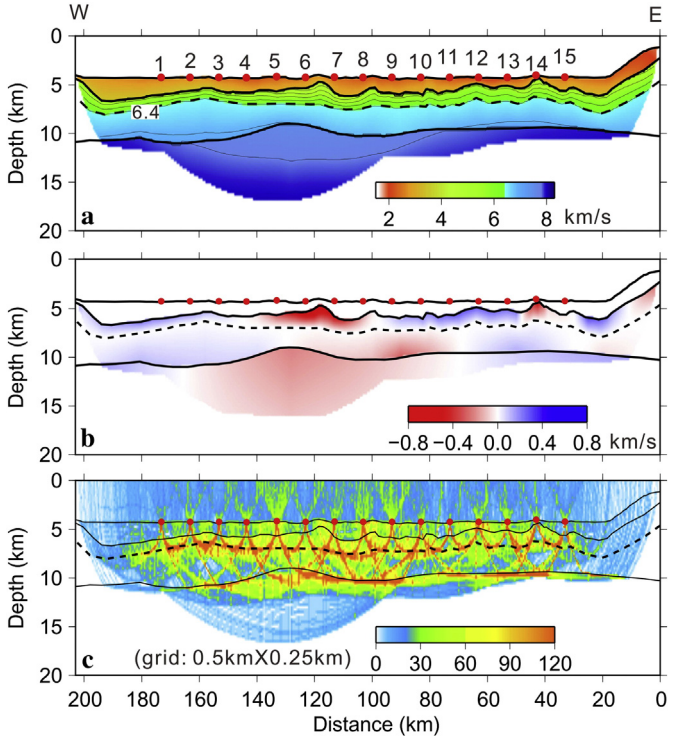

Fig. 10. The crustal structure model of profile OBS2013-ZN. (a) The P-wave velocity model. The solid black lines represent seafloor, sediment basement and the Moho discontinuity, respectively. The dashed black line indicates the interface between the oceanic layer 2 and layer 3. The thin black lines represent isovelocity contours with interval of 0.3 km/s. The numbered solid red circles represent OBS stations. (b) The velocity perturbation anomaly. (c) The ray density distribution (calculation grid: 0.5 km × 0.25 km).

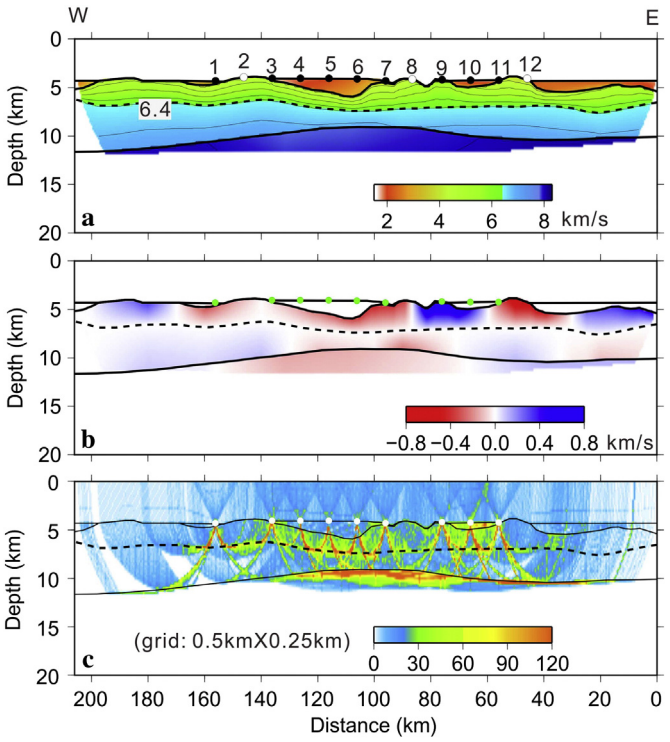

Fig. 11. The crustal structure model of profile OBS2014-ZN. (a) The P-wave velocity model. (b) The velocity perturbation anomaly. (c) The ray density distribution. The other illustrations are same as that in Fig. 10.

Table 2
Uncertainties of layer velocities and interfaces in the models.

Profile	OBS2013-ZN	OBS2014-ZN
Top velocity of sedimentary layer	±0.15 km/s	±0.20 km/s
Bottom velocity of sedimentary layer	±0.13 m/s	±0.20 km/s
Top velocity of crust	±0.20 km/s	±0.22 km/s
Bottom velocity of crust	±0.30 km/s	±0.22 km/s
Depth of basement	±0.15 km	±0.10 km
Depth of Moho	±0.28 km	±0.25 km

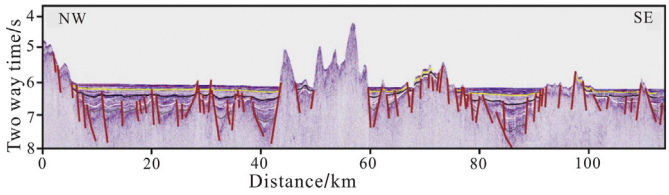

Fig. 12. A multi-channel seismic profile crossed the Zhongnan Fault. It indicates numerous high-angle extensional faults forming fracture zones along the profile (Jin et al., 1989).

presence of a low velocity zone of 7.7 km/s in the uppermost portion of the mantle under these stations.

5. Discussion

Although the SCS sea basin sediment is only 1–2 km thick, we cannot distinguish faults directly from the seismic sections of the two wide-angle OBS profiles by finding sharp local phase Pg drops that are usually related to major faults. Nevertheless, some multiple channel seismic profiles obtained in previous investigations indicated the presence of a dense distribution of faults (Fig. 12) (Jin et al., 1989; Li et al., 2011). The large number of faults and fractures in the transform fault zone probably explains the low velocity zones observed in both the upper crust and the upheaving part of the mantle (Fig. 10b and Fig. 11b).

The thin crust with low velocity has been observed in major mid-ocean ridges, and is usually related to the thermal effect of the offsets of the accretionary segments by the transform fault (Whitmarsh and Calvert, 1986). Near transform faults along min-ocean-ridge, mantle melting is reduced by conductive cooling, and less crust is produced (White et al., 2001; Minshull et al., 2006). This is especially true at slow-spreading reidges. The crustal thinning observed along our profiles is probably due to this effect. Therefore, we suggest that the shallow low velocity zone in the crust is composed of various small faults that form a wide fracture zone. A NW-SE orientation of the fracture zone (40–60 km wide) is suggested by the offset of the upheaval portions of the Moho in the two profiles (Fig. 13). This result roughly agrees with that (with width > 30 km) postulated by Franke et al. (2011) but different from the N-S trending fault proposed by Ru and Piggot (1986) and Yao (1995).

The faults or fractures formations were controlled by varied stress fields during the multi-episode evolution of the SCS sea basin (Briais et al., 1993; Li et al., 2011). A nearly N-S spreading direction at the beginning of the opening of the South China Sea, and then a NW-SE direction, with propagation to the southwest, has been suggested by Briais et al. (1993), combining magnetic anomaly analysis and a few multi-beam bathymetry swaths providing the orientation of the abyssal hills. Therefore we suggest that the NW-SE-trending fracture zone revealed by our velocity models was formed during the break-up of the Macclesfield-Reed Bank when spreading propagated southwestward. For its trending direction is consistent with the NW-SE spreading of the southwest sub-basin. The study of multibeam bathymetry and magnetic anomalies (Pautot et al., 1986; Briais et al., 1989, Briais et al., 1993) also suggested that when Macclesfield-Reed Bank block was split into two pieces at approximately 25 Ma, the spreading direction changed from NS to SE and resulted in the direction change of the major transform fault in the vicinity of the Macclesfield and Reed Banks.

6. Conclusions

Based on the data from two wide-angle seismic profiles of OBS at the central basin of the SCS that trend E-W at 15.1°N and 14.5°N

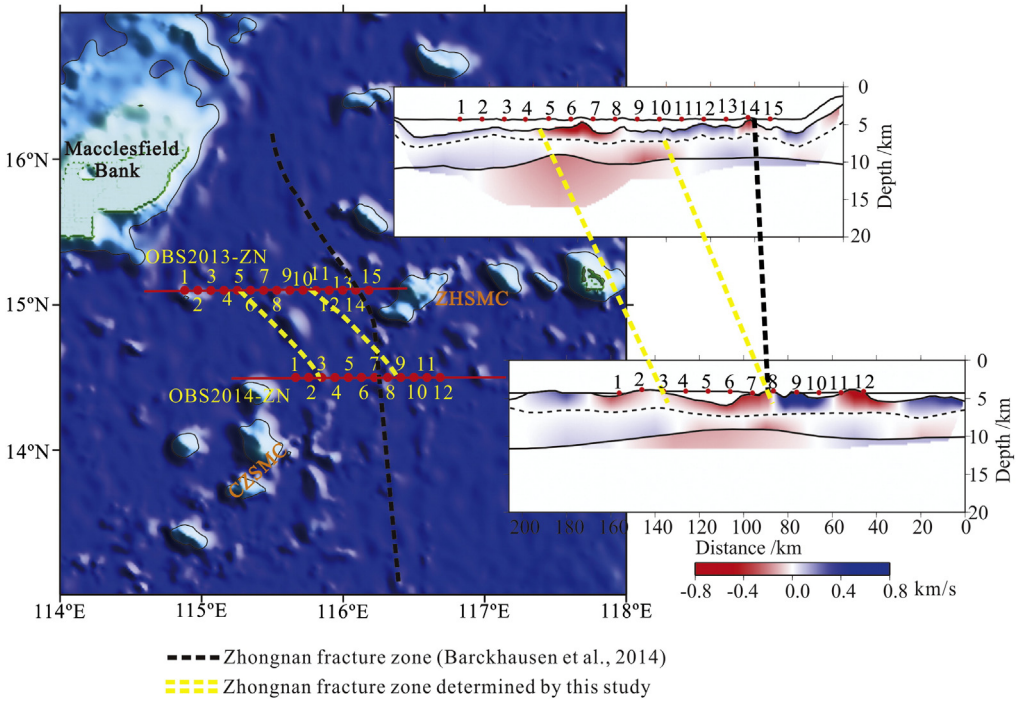

Fig. 13. The location of a NW-SE-trending fracture zone separating the southwest sub-basin from the east sub-basin It is plotted according to the right two insets of velocity anomaly models simulated by this study (Fig. 10b and Fig. 11b), as well as the seabed relief.

respectively and cross the Zhongnan fault, we determined the oceanic crust thickness, P-wave velocity structures and Moho discontinuity variations using 2D ray-tracing and draw the following conclusions:

(1) The oceanic basin of the SCS has a typical oceanic crust covered by a 1–2 km thick sediment layer with a velocity of 2.0–3.5 km/s. The crust has a thickness of 5–8 km, of which oceanic layer 2 is 1.8–3 km thick, with velocity increasing downward from 4.3 km/s to 6.4 km/s, and oceanic layer 3 is 3–5 km thick, with velocity increasing downward from 6.4 km/s–7.0 km/s. The oceanic basin Moho depth is approximately 6 km below seabed.
(2) The Moho discontinuity has an obvious upheaval zone with a low velocity of 7.6 km/s, which corresponds to the low velocity zone in oceanic layer 2. The offset in longitude of the zones of thinner crust observed in our profiles suggests a NW-SE orientation of the transform zone.
(3) The NW-SE orientation Zhongnan transform fault zone in our study area is consistent with the direction of opening of the South China Sea in the last stage of its evolution. This large transform fault zone connected and offset the spreading centers of the east and southwest sub-basin.

Acknowledgements

We are grateful to the scientists who joined the cruise, especially Dr. Sun. Jin-long and Dr. Huang Hai-bo and the crew of the R/V "*Shiyan 2*". The seismic experiments and our researches are supported by the National Natural Science Foundation of China (grants 91228205, 41176046 and 41406052), the National Basic Research program of China (grant 2012CB417301) and Scientific Research Fund of the Second Institute of Oceanography, State Oceanic Administration (JG1413). We used the RayInvr code (Zelt and Smith, 1992) for seismic inversion. Some of our figures were plotted using GMT (Wessel and Smith, 1995). We thank Dr. Anne Briais and an anonymous reviewer for their constructive comments.

References

Ao, W., Zhao, M.H., Qiu, X.L., Li, J.B., Ruan, A.G., Li, S.J., Zhang, J.Z., 2010. The correction of shot and OBS position in the 3D seismic experiment of the SW Indian Ocean ridge. Chin. J. Geophys. 53 (6), 1072–1081.
Braitenberg, C., Wienecke, S., Wang, Y., 2006. Basement structures from satellite-derived gravity field: South China Sea ridge. J. Geophys. Res. 111, 1–15, B05407.
Briais, A., Tapponnier, P., Pautot, G., 1989. Constraints of Seabeam data on crustal fabrics and seafloor spreading in the South China Sea, Earth Planet. Sci. Lett. 95, 307–320.
Briais, A., Patriat, P., Tapponnier, P., 1993. Updated interpretation of magnetic anomalies and seafloor spreading in the South China Sea:implications for the Tertiary tectonics of Southeast Asia. J. Geophys. Res. 98 (B4), 6299–6328.
Franke, D., 2013. Rifting, lithosphere breakup and volcanism: comparison of magma-poor and volcanic rifted margins. Mar. Pet. Geol. 43, 63–87.
Franke, D., Barckhausen, U., Baristeas, N., Engels, M., Ladage, S., Lutz, R., Montano, J., Pellejera, N., Ramos, E.G., Schnabel, M., 2011. The continent-ocean transition at the southeastern margin of the South China Sea. Mar. Pet. Geol. 28, 1187–1204.
Hékinian, R., Bonté, P., Pautot, G., Jacques, D., Labeyrie, L.D., Mikkelsen, N., Reyss, J.L., 1989. Volcanics from the South China Sea ridge system. Oceanol. Acta 12 (2), 101–115.
Hutchison, C.S., 1989. Geological evolution of Southeast Asia. In: Oxford Monographs on Geology and Geophysics, 13. Clarendon Press, Oxford.
IODP Expedition 349 Scientists, 2014. South China Sea tectonics: opening of the South China Sea and its implications for southeast Asian tectonics, climates, and deep mantle processes since the late Mesozoic. International Ocean Discovery Program Preliminary Report. 349.
Jin, X.L., Lu, W.Z., Ke, C.Z., 1989. Geoscience Research Report of the South China Sea. J. East China Sea 7 (4), 20–29 (In Chinese).
Kudrass, H.R., Wiedicke, M., Cepek, P., Kpeuzer, H., Muller, P., 1986. Mesozoic and Cainozoic rocks dredged from the South China Sea (Reed Bank area) and Sulu Sea and their significance for plate-tectonic reconstructions. Mar. Pet. Geol. 3, 19–30.
Li, C.F., Song, T., 2012. Magnetic recording of the Cenozoic oceanic crustal accretion and evolution of the South China Sea basin. Chin. Sci. Bull. 57, 3165–3181.
Li, C.F., Zhou, Z.Y., Li, J.B., Chen, B., Geng, J., 2008. Magnetic zoning and seismic structure of the South China Sea ocean basin. Mar. Geophys. Res. 29, 223–238.
Li, J.B., DING, W.W., Gao, J.Y., Wu, Z.Y., Zhang, J., 2011. Cenozoic evolution model of the sea-floor spreading in South China Sea: new constraints from high resolution geophysical data. Chin. J. Geophys. 54 (6), 894–906.
Li, C.F., Xu, X., Lin, J., Sun., Z., Zhu, J., Yao, Y., X.X., Z., Liu, Q.S., Kulhanek, D.K., Wang, J., Song, T.R., Zhao, J.F., Qiu, N., Guan, Y.X., Zhou, Z.Y., Williams, T., Bao, R., Briais, A., Brown, E.A., Chen, Y.F., Clift, P.D., Colwell, F.S., Dadd, K.A., Ding, W.W., Almeida, I.H., Huang, X., Hyun, S., Jiang, T., Koppers, A.A.P., Li, Q.Y., Liu, C.L., Liu, Z.F., Nagai, R.H., Peleo-Alampay, A., Su, X., Tejada, M.L.G., Trinh, H.S., Yeh, Y.C., Zhang, C.L., Zhang, F., Zhang, G.L., 2014. Ages and magnetic structures of the South China Sea constrained by deep tow magnetic surveys and IODP Expedition 349. Geochem. Geophys. Geosyst. 15 (12), 4958–4983.
Ludwig, W.J., Kumar, N., Houtx, R.E., 1979. Profiler-Sonobuoy measurements in the South China Sea Basin. J. Geophys. Res. 84 (B7), 3505–3518.
Minshull, T., Muller, M., White, R., 2006. Crustal structure of the Southwest Indian Ridge at 66°E: 248 seismic constraints. Geophys. J. Int. 166, 135–147.
Pautot, G., Rangin, C., Briais, A., Tapponnier, P., Beuzart, P., Lericolais, G., Mathieu, X., Wu, J., Han, S., Li, H., Lu, Y., Zhao, J., 1986. Spreading direction in the central South China Sea. 321 (8), 150–154.
Qiu, X.L., Zhao, M.H., Ao, W., Lv, C.C., Hao, T.Y., You, Q.Y., Ruan, A.G., Li, J.B., 2011. OBS survey and crustal structure of the Southwest Sub-basin and Nansha Block, South China Sea. Chin. J. Geophys. 54 (6), 1009–1021.
Ruan, A.G., Niu, X.W., Qiu, X.L., Li, J.B., Wu, Z.L., Zhao, M.H., Wei, X.D., 2011. A wide angle ocean bottom seismometer experiment across Liyue Bank, the southern margin of the South China Sea. Chin. J. Geophys. 54 (6), 1033–1044.
Ru, K., Piggot, J.D., 1986. Episodic rifting and subsidence in the South China Sea. A.A.P.G. Bull. 70 (9), 1136–1155.
Sun., Z., Zhou, D., Wu, S.M., Zhong, Z.H., Keep, M., Jiang, J.Q., Fan, H., 2009. Patterns and dynamics of rifting of passive continental margin from self to slope of the northern South China Sea: evidence from 3D analogue modeling. J. Earth Sci. 20 (1), 137–146.
Taylor, B., Hayes, D.E., 1980. The tectonic evolution of the South China Sea Basin. In: Hayes, D.E. (Ed.), The Tectonic and Geologic Evolution of Southeast Asian Seas and IslandsGeophys. Monogr. 23. AGU, Washington, D.C., pp. 89–104.
Taylor, B., Hayes, D.E., 1983. Origin and history of South China Sea Basin. In: Hayes, D.E. (Ed.), The Tectonic and Geologic Evolution of Southeast Asian Seas and IslandsGeophys. Monogr. 27. AGU, Washington, D.C., pp. 23–56.
Wang, X.J., Wu, M.Q., Liang, D.H., Yin, A.W., 1984. Some geochemical characteristics of basalts in the South China Sea. Chin. J. Geochem. 4332–4,340.
Wessel, P., Smith, W.H., 1995. New version of generic mapping tools released. Eos. Trans. Am. Geophys. Union 76 (33), 329.
White, R.S., McKenzie, D., O'Nions, R.K., 1992. Oceanic crustal thickness from seismic measurements and rare earth element inversions. J. Geophys. Res. 97, 19,683–19,715.
White, R.S., Minshull, T.A., Bickle, M., Robinson, C.J., 2001. Melt generation at very slow-spreading oceanic ridges: Constraints from geochemical and geophysical data. J. Petrol. 42, 1171–1196.
Whitmarsh, R.B., Calvert, A.J., 1986. Crustal structure of Atlantic fracture zones-I. The Chailie-Gibbs Frature Zone. J. Geophys. Res. 85, 107–138.
Xu, Y.G., Wei, J.X., Qiu, H.N., Zhang, H.N., Huang, X.L., 2012. Opening and evolution of the South China Sea constrained by studies on volcanic rocks: preliminary results and a research design. Chin. Sci. Bull. 57 (24), 3150–3164.
Yan, Q.S., Shi, X.F., Wang, K.S., Bu, W.R., Xiao, L., 2008. Major element, trace element, Sr–Nd–Pb isotopic studies of Cenozoic alkali basalts from the South China Sea. Sci. China Ser. Earth Sci. 51 (4), 550–566.
Yan, Q.S., Shi, X.F., Paterno, R.C., 2014. The late Mesozoic-Cenozoic tectonic evolution of the South China Sea: a petrologic perspective. J. Asian Earth Sci. 85, 178–201.
Yao, B.C., 1995. Characteristics and tectonic meaning of Zhongnan-Lile fault. Geogr. Res. South China Sea 1–14 (Memoir 7).
Yao, B., Zeng, W., Hayes, D.E., Spangler, S., 1994. The Geological Memoir of South China Sea Surveyed Jointly by China and USA: Wuhan. China Univ. Geosci. Press (in Chinese).
Zelt, C., Smith, R., 1992. Seismic traveltime inversion for 2-D crustal velocity structure. Geophys. J. Int. 99, 16–34.
Zelt, C., 1999. Modeling strategies and model assessment for wide-angle seismic travel time data. Geophys. J. Int. 139, 183–204.